Pattern formation at the bicritical point of the Faraday instability

C. Wagner,[1] H.-W. Müller,[2] and K. Knorr[1]

[1]*Institut für Technische Physik, Universität des Saarlandes, Postfach 151150, D-66041 Saarbrücken, Germany*
[2]*Max Planck Institut für Polymerforschung, Ackermannweg 10, D-55128 Mainz, Germany*

We present measurements on parametrically driven surface waves (Faraday waves) performed in the vicinity of a bicritical point in parameter space, where modes with harmonic and subharmonic time dependence interact. The primary patterns are squares in the subharmonic and hexagons in the harmonic regime. If the primary instability is harmonic we observe a hysteretic secondary transition from hexagons to squares without a perceptible variation of the fundamental wavelength. The transition is understood in terms of a set of coupled Landau equations and related to other canonical examples of phase transitions in nonlinear dissipative systems. Moreover, the subharmonic-harmonic mode competition gives rise to a variety of new superlattice states. These structures are interpreted as mediator modes involved in the transition between patterns of fourfold and sixfold rotational symmetry.

The Faraday experiment has nowadays become a model system for pattern formation in hydrodynamic systems [1]. Standing waves are generated on the liquid air interface in response to a time periodic gravity modulation. Under typical laboratory conditions and assuming that the excitation acceleration is sinusoidal with $g(t)=g_0+a\sin\Omega t$ these surface waves oscillate with twice the period of the external drive [2]. This is a consequence of the parametric drive mechanism and denoted here as the *subharmonic* Faraday resonance. Surface waves synchronous (*harmonic*) with the drive can be generated, too. They have been observed first by adding a second frequency component to the excitation signal [3]. Later on, following a suggestion of Kumar [4], harmonic Faraday waves have also been excited with the usual single frequency drive [5]. This, however, requires rather extreme (parameter) conditions, namely thin fluid layers in combination with drive frequencies lower than some threshold f_b. Increasing $f=\Omega/(2\pi)$ beyond f_b lets the Faraday waves resonate with their usual subharmonic time dependence [6]. For operating frequencies f close to the bicritical value f_b the harmonic and subharmonic modes compete. Owing to the dispersion of surface waves different frequencies imply different wavelengths. As a consequence nonlinear pattern formation is affected in a significant manner: In our experiments subharmonic modes ($f>f_b$) form square patterns, harmonic modes ($f<f_b$) hexagons. For the latter we observe a transition towards a square pattern at elevated drive amplitude. This is similar to the canonical hexagon-line transition in Rayleigh-Bénard convection, which can be observed if "non-Boussinesq" effects become significant [7,8]. A transition from hexagons to squares has been found only recently in the Bénard Marangoni instability [9–12].

The measurements presented here give a comprehensive account of our investigations on Faraday pattern selection in the vicinity of the bicritical point. Thereby the interaction between harmonic and subharmonic modes of different wavelengths gives rise to new resonant phenomena: superlattices with either fourfold or sixfold rotational invariance. Though superlattices are very common in solid state and surface physics, they have been found on macroscopic scales only recently [6,13–16].

Within a cascade of secondary phase transitions superlattices are found to mediate between the two incompatible symmetry classes, of squares and hexagons. For instance a primary subharmonic pattern with quadratic surface tiling experiences a crossover to a hexagonal superlattice via two quadratic superlattices [6] with a prominent displacive character in one or two lateral directions. After passing a phase with a hexagonal superlattice the transition process reaches a pure hexagonal pattern characterized by a single wavelength and oscillating in synchronous response to the external drive.

For several of the observed transitions we are able to provide explanations in terms of resonant amplitude equations for the governing spatial modes. The structure of these equations is simply based on symmetry and resonance arguments. In spite of their simplicity these equations provide an understanding of many remarkable features of the superlattices, in particular their displacive character. This phenomenological approach is certainly facilitated by the small number of experimental control parameters. This is unlike earlier experiments [14–16], which use a more complicated multiple frequency drive or a viscoelastic fluid to drive the system into the bicritical situation. Thereby different kinds of superlattices have been reported as well. But clearly, a larger number of control parameters renders a theoretical understanding more unwieldy and less intuitive. For the theoretical approach to superlattices see, e.g., Ref. [17].

I. EXPERIMENTAL SETUP

A. Vibration system and sample fluid

Figure 1 shows a schematic diagram of the experimental setup. Its heart is a large displacement shaker unit (V617 Gearing & Watson Electronics Ltd.) connected to a 4 kW power amplifier. The shaker supplies a maximum force of 4670 N and a peak-to-peak elevation of $s_{max}=54$ mm. Such a large displacement is necessary to obtain a sufficient acceleration a at lower driving frequencies. The drive signal for the power amplifier is synthesized by means of a digital-analog card installed in a Pentium PC. The actual acceleration of the container is measured with a piezoelectric device,
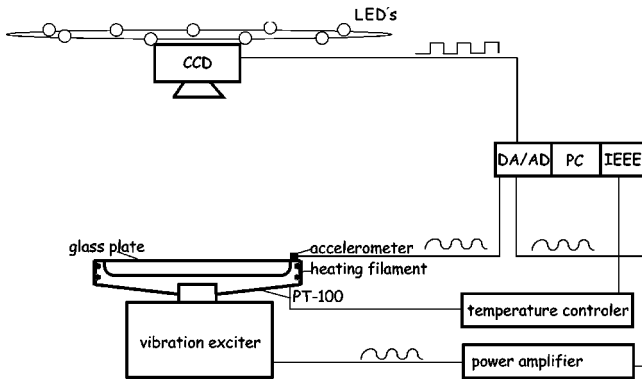
FIG. 1. Sketch of the experimental setup. See text for further explanation.

the amplified signal of which is routed to the PC for data acquisition. Since the characteristics of the shaker turned out to be rather nonlinear at operation frequencies below $f = \Omega/(2\pi) < 10$ Hz a continuous control of the excitation signal was necessary. To guarantee a sinusoidal container acceleration $a \sin \Omega t$ the recorded accelerometer signal was decomposed into Fourier components. The parasitic higher harmonics of Ω were eliminated by admixing Fourier contributions with appropriate inverse phases to the excitation signal. Their amplitudes were determined by a proportional control loop. That way the power spectrum of the accelerometer signal is made monochromatic with a purity of 99%.

The cylindrical container for the sample liquid was machined out of aluminum and was anodized black. To avoid pollution and temperature drifts within the fluid, the container was sealed with a glass plate. The inner container diameter was $d = 290$ mm, the depth 50 mm. Over a distance of 12 mm from the edges of the container the depth continuously increased from zero to the bottom. This "soft boundary condition" with an average angle of 30° helped to minimize the generation of parasitic meniscus waves. A meniscus under vertical vibration always emits waves with the frequency f of the external drive. Since these waves have non vanishing amplitudes even at subcritical drive amplitudes $a < a_c$ they blur the onset detection. The beachlike boundary fulfilled their purpose well, at least above 10 Hz.

The probe fluid was a low viscosity silicon oil (Dow Corning 200) with the manufacturer specifications of kinematic viscosity $\nu = 5 \times 10^{-6}$ m²/s, surface tension $\sigma = 0.0194$ N/m, and density $\rho = 920$ kg/m³ at our working temperature $T = 25$ °C. A heating foil was mounted on the outside of the container. By means of a temperature controller the temperature measured by a PT-100 resistor (embedded in the container body) was regulated by ± 0.1 °C.

B. Visualization technique

To visualize the surface profile we used a full frame CCD camera (Hitachi KPF-1) situated above the fluid surface in the center of a ring consisting of 120 LEDs. The ring had a radius of $R = 0.3$ m and its distance from the fluid surface was $L = 1.50$ m. The camera was synchronized to the excitation signal with an exposure time of 1/256 of the drive

period. It follows from geometrical optics that only surface elements with a certain steepness reflect light into the camera.

For an evaluation of the spatial symmetry of the surface deformation $\zeta(x,y)$ we relied on a Fourier technique. To that end the recorded light intensity $I(x,y)$ of a video image was convoluted with a Gaussian window function and processed by a FFT algorithm. This yields the two-dimensional spatial power spectrum $P(\mathbf{k})$. To determine the wavelength of the pattern $P(\mathbf{k})$ was azimuthally averaged by integrating over circles with constant radius $|\mathbf{k}| = k$. The primary peak in the resulting one-dimensional spectrum was fitted by a Gauss function the center of which determines the fundamental wave number. Clearly, the resolution of this procedure is limited by the number of wavelengths in the container. This is especially the case for subharmonic Faraday waves where the uncertainty of $\Delta k/k$ is about 10%.

Due to the nonlinear relationship between the surface elevation $\zeta(x,y)$ and the recorded light intensity $I(x,y)$, the power spectrum entails higher harmonics of the fundamental wave number, even if the surface profile $\zeta(x,y)$ does not. Thus the relation between $I(x,y)$ and $\zeta(x,y)$ is generally too complicated to allow a reconstruction of the surface profile. Nevertheless for simple surface patterns (such as squares) we have solved this "inverse problem" by the following method: Starting from an estimated surface profile composed of a small number of spatial Fourier modes, the light distribution of the expected video image was computed by means of a ray tracing algorithm. Then we adapted the mode amplitudes and their relative phases such as to optimize the agreement between the calculated and recorded video picture.

A reconstruction of the full time dependence of an oscillating surface wave pattern was not possible with our equipment. Nevertheless, the electronic shutter of the camera provides an easy and very sensitive technique to discriminate subharmonic frequency components in an otherwise harmonic time signal. This is because a harmonic time dependence $\zeta^h(t)$ is invariant under the symmetry operation $t \to t + 2\pi/\Omega$ implying a frequency spectrum of integer multiples of Ω thus $\zeta^h(t) = \Sigma_n \zeta_n e^{in\Omega t}$. In contrast the subharmonic time signal transforms after one drive period as $\zeta^s \to -\zeta^s$ enforcing a Fourier representation in the form of $\zeta^s(t) = \Sigma_n \zeta_n e^{i[(n+1/2)\Omega t]}$. Thus by triggering the camera shutter with the drive frequency Ω, video images with a harmonic time dependence appear stationary, while those with subharmonic frequency contributions flicker due to a slight optical asymmetry between heaps and hollow of the deformed surface. Note however, that this trigger technique does not allow to identify harmonic frequency components in an otherwise subharmonic spectrum.

II. THE ONSET OF THE FARADAY INSTABILITY

It is well known that the stability problem of a free liquid surface under gravity modulation (Faraday instability) can be approximately mapped to that of a parametrically driven pendulum [18,2]. The primary resonance of which occurs at twice the period of the drive (*subharmonic response*). How-
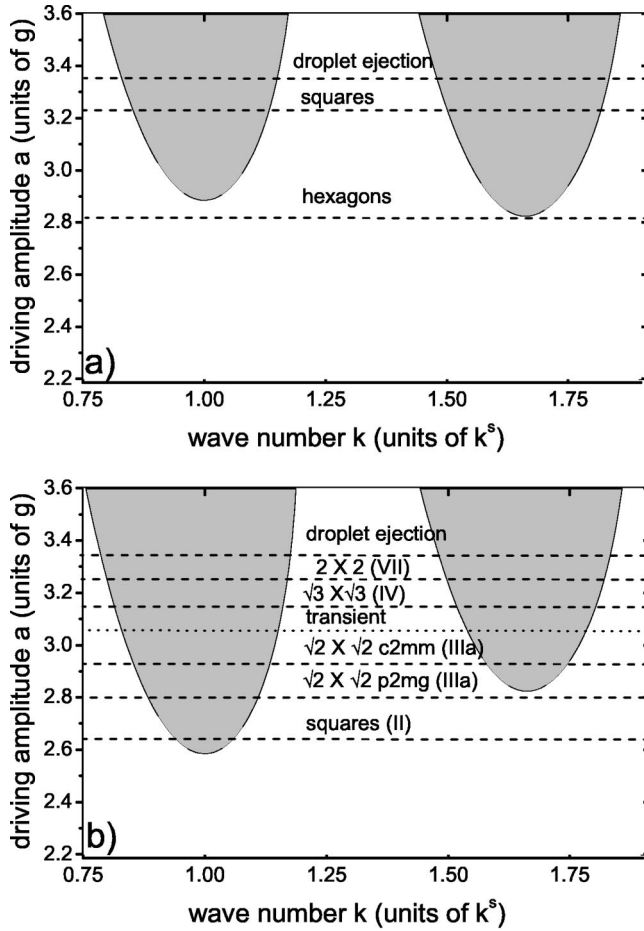
FIG. 2. Neutral stability curves $a(k)$ computed for the parameters of the sample fluid at a drive frequency (a) $f=6.25$ Hz$<f_b$ and (b) $f=7.25$ Hz$>f_b$. In (a) the primary resonance is harmonic; in (b) it is subharmonic. Regions where the flat surface state is unstable are shaded. Horizontal lines denote the thresholds for secondary and higher order transitions shown in Fig. 4.

ever, as first pointed out by Kumar [4] the Faraday instability may also appear in synchronous resonance with the external drive, usually denoted as the *harmonic* response. The conditions under which the harmonic resonance preempts the subharmonic one have been worked out in detail by Cerda and Tirapegui [19] and Müller *et al.* [5] revealing that low filling levels in combination with small drive frequencies are necessary. In the present experiment we choose a fill height of $h=0.7$ mm, which is—at the operation frequencies of $6<f<8$ Hz—comparable to the viscous penetration depth $\kappa=\sqrt{2\nu/\Omega}\approx0.5$ mm. For the fluid parameters at hand a linear stability analysis of the flat surface state (according to the method of Kumar and Tuckermann [20], which assumes a laterally infinite system) reveals the location of the bicritical point at a drive frequency of $f_b=6.3$ Hz. Figure 2 shows neutral stability diagrams (drive amplitude a vs wave number k) for both situations $f<f_b$ and $f>f_b$.

Experimentally the critical acceleration a_c (absolute minimum of the neutral stability diagram) has been determined by setting up the system at a constant frequency and ramping a quasistatically in steps of 0.2% suspended by intervals of 240 s. The onset amplitude a_c was defined when the camera detected the first light reflex [Fig. 3(a)]. To enhance the detection sensitivity the surface was illuminated by a diffusive light source from the side rather than using the dark-field technique described above. This is because the latter method requires a minimum surface gradient of $|\nabla\zeta(x,y)|=\tan\alpha\approx0.1$ for the onset detection. We estimate the accuracy of our threshold determination by 0.5%.

Once a standing wave pattern had covered the whole surface the fundamental frequency of the surface oscillation was determined with the help of the electronic shutter of the video camera. That way we located the transition point at a bicritical frequency $f_b=6.5\pm0.1$ Hz. After these preliminary measurements we switched back to the dark-field illumination to proceed with the spatial pattern analysis. The critical wave numbers k_c^h and k_c^s, respectively, were determined by Fourier transforming a surface image taken at a driving strength of $\varepsilon=(a-a_c/a_c)\approx0.03$ [Fig. 3(b)]. The operating prescription $k_c=k(\varepsilon\approx0.03)$ for the determination of the critical wave number is motivated by the fact that we were unable to detect any change of the wave number k by varying ε (see also [21]). The experimental results for a_c and k_c as well the bicritical frequency f_b are found to be in good agreement with the theoretical predictions. For the critical acceleration the discrepancy is less than 2%. Here the uncertainty is mainly due to errors in the determination of the small fill height h. For larger values of h the agreement improves up to 1%. For the critical wave number the discrepancy between theory and experiment is better than 4% in the harmonic case but it increases up to 10% on the subharmonic regime. This is due to the spatial resolution, which becomes worse at larger wavelength.

Owing to the abrupt change of the response frequency at $f=f_b$ the wave number shows a discontinuous jump [see Fig. 3(b)]. The empiric ratio of the wave numbers at $f=f_b$ is found to be

$$\left.\frac{k_c^h}{k_c^s}\right|_{expt}=1.58\pm0.15, \tag{1}$$

in agreement with the prediction of the linear stability theory $k_c^h/k_c^s|_{theor}=1.59$. The latter can be approximated by the (nonviscous) finite depth dispersion relation yielding $k^h/k^s|_{disp}=1.81$.

We finally checked if the correlation length $\xi=2\pi/\delta k$ would not exceed the container diameter. δk is the bandwidth of the unstable modes, given by the shaded region in Fig. 2. ξ diverges for $\epsilon\rightarrow0$ and for sufficient small ϵ the correlation length remains always larger than the container diameter and the pattern is largely determined by the container symmetry [28]. However, in our experiments the damping from the bottom is sufficiently strong and the bandwidth of the unstable modes already yields at $\varepsilon=0.01$ a correlation length shorter than the container diameter. All remaining influences of the container symmetry on the pattern dynamics observed in our experiments is thus to attribute to a different aspect ratio, the ratio of the container size to the wavelength.
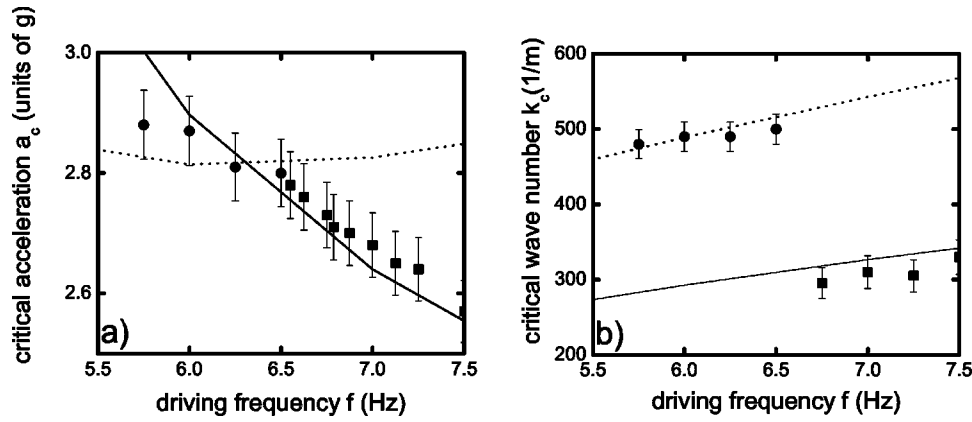
FIG. 3. (a) Critical amplitude a_c and (b) critical wave number k_c for the onset of the Faraday instability drawn as a function of the drive frequency f. The bicritical point $f=f_b$ is located where the harmonic ($f<f_b$) and subharmonic ($f>f_b$) thresholds intersect. Symbols mark experimental data points; lines mark the theoretical results for a laterally infinite fluid layer. Circles and dotted lines refer to the harmonic response, and squares and solid lines to the subharmonic one.

III. OVERVIEW OF THE PHASE DIAGRAM

The phase diagram shown in Fig. 4 has been obtained at various constant driving frequencies $f=\Omega/(2\pi)$ while ramping the driving amplitude from $\varepsilon=-0.01$ up to $\varepsilon=0.25$ in steps of $\Delta\varepsilon=-0.002$. After each increment the ramp was suspended for 240 s to give the system time to relax. Then a photo or—in the case of time dependent patterns a video film—of the surface state was taken. At the point where a new spatial or temporal mode appeared or an existing one died out, the actual acceleration was defined as the transition boundary to a new "phase." At the maximum acceleration amplitude the ramp was reversed to check for an eventual hysteresis.

In Sec. IV we describe in detail the type of primary patterns, which appear near onset of the Faraday instability. Second- and higher-order transitions towards more complicated structures are dealt with in Secs. V and VI. Thereby two representative experimental runs will be described in detail, the first was taken at $f=6.25$ Hz$<f_b$ and a second at $f=7.25$ Hz$>f_b$.

In the former case the primary pattern exhibits a harmonic time dependence, which turns out to be quite robust as it persists over the whole investigated ε ramp. The primary spatial surface wave structure starts with an ideal hexagonal symmetry (region V), which then transforms into a pattern of squares (region VI) as ε is raised. This transition is hysteretic, its global aspects can be understood in terms of a simple model of six coupled amplitude equations.

In the second run at $f>f_b$ the primary surface pattern consists of subharmonically oscillating squares (region II). On increasing the drive strength ε the interaction with the neighboring harmonic Faraday instability leads to the appearance of a quadratic $\sqrt{2}\times\sqrt{2}$ superlattice with a displacive character in one and/or two lateral directions (regions IIIa and IIIb, respectively). Displacive means that rows of wave crests are shifted to each other. After crossing a phase region of nonstationary patterns with a slow time dependence the system enters a hexagonal $\sqrt{3}\times\sqrt{3}$ superlattice (region IV). Mediated by a second local reconstruction pro-

cess the final stationary surface pattern is a quadratic 2×2 superlattice (region VII). Regardless of whether the response is s or h, the surface finally breaks up and droplets are ejected (region VIII, $\varepsilon\simeq0.15$–0.25).

IV. PATTERN FORMATION CLOSE ABOVE ONSET OF THE FARADAY INSTABILITY

Close to the harmonic onset ($f<f_b$) hexagons are the preferred primary surface pattern [Fig. 5(a), region V]; however, for $f>f_b$ squares are stable [Fig. 9(a), region II]. Wagner, Müller and Knorr [6] (see Fig. 3 therein) have shown that even for small ε the wave profile is rather anharmonic.

A. Theoretical model for the primary hexagonal pattern at $f<f_b$

The appearance of hexagons at the "harmonic side" of the bicritical point follows from a triple wave vector resonance. A normal form for the surface deformation profile is given by

$$\zeta(\mathbf{r},t)=\left[\sum_m\left\{\begin{array}{l}H_m e^{i\mathbf{k}_{H_m}\cdot\mathbf{r}}\\S_m e^{i\mathbf{k}_{S_m}\cdot\mathbf{r}}\end{array}\right\}+\text{c.c.}\right]$$
$$\times\sum_{n=-\infty}^{+\infty}\zeta_n\left\{\begin{array}{ll}e^{in\Omega t}&\text{for}\quad h\quad\text{response}\\e^{i(n+1/2)\Omega t}&\text{for}\quad s\quad\text{response.}\end{array}\right.\quad(2)$$

Here $\mathbf{r}=(x,y)$ is the horizontal coordinate, the lateral wave vectors $\mathbf{k}_{H_m}$ and $\mathbf{k}_{S_m}$, with $|\mathbf{k}_{H_m}|=k^h$ and $|\mathbf{k}_{S_m}|=k^s$ composing the spatial pattern and the ζ_n are the temporal Fourier coefficients determined by the linear stability problem. Feeding ζ and a similar ansatz for the hydrodynamic velocity field into an arbitrary quadratic nonlinearity results in a frequency spectrum of integral multiples of Ω, whether or not S or H are considered. Thus quadratic nonlinearities are able to resonate with *harmonic* linear eigenmodes, but not with *subharmonic* ones. Clearly, spatial resonance must
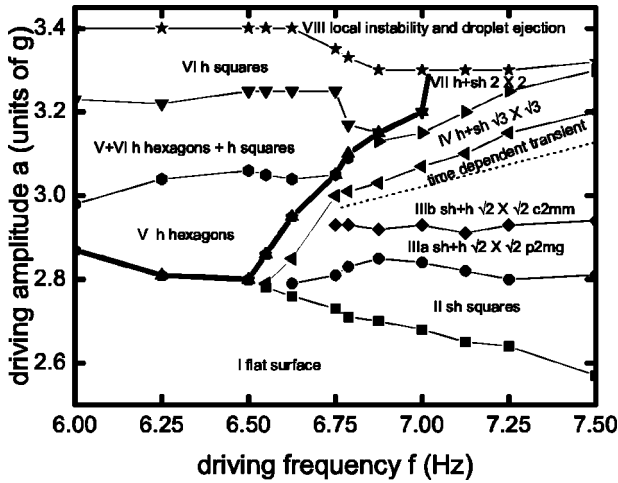
FIG. 4. Phase diagram of the observed patterns obtained by quasistatically ramping the driving force. The symbols mark the observed transition points between the different patterns; the lines are guides for the eyes. The spatial ordering of the patterns is indicated by roman numerals, the arabic letters s and h denote the character of the time dependence being either purely subharmonic or harmonic. The $s+h$ label indicates patterns formed by a interaction of subharmonic and harmonic modes. The thick line separates harmonic from subharmonic and $s+h$ regions. I: flat surface; II: subharmonically oscillating squares [Figs. 9(a) and 9(b)]; IIIa: $\sqrt{2} \times \sqrt{2}$ superlattice p2mg [Figs. 9(c) and 9(d)]; IIIb: $\sqrt{2} \times \sqrt{2}$ superlattice c2mm [Figs. 9(e) and 9(f)]; within the subregion above the dotted line the pattern is time dependent and disordered (see Fig. 12); IV: $\sqrt{3} \times \sqrt{3}$ superlattice (only for $f < 6.9$ Hz stationary, Fig. 13); V: harmonically oscillating hexagons [Fig. 5(a)]; VI: harmonically oscillating squares [Fig. 5(d)]; VII: 2×2 superlattice (Fig. 14); VIII: local instability and droplet ejection.

be granted as well. The requirement $|\mathbf{k}_{H_1}| = |\mathbf{k}_{H_2}| = |\mathbf{k}_{H_3}| = k_c^h$ along with the resonance condition $\mathbf{k}_{H_1} + \mathbf{k}_{H_2} + \mathbf{k}_{H_3} = \mathbf{0}$ enforce a mutual angle of 120° between the wave vectors implying the hexagonal symmetry. The evolution equations for the respective mode amplitudes H_1, H_2, H_3 are of the following structure:

$$\partial_t H_1 = \varepsilon H_1 + \beta H_2^\star H_3^\star - [|H_1|^2 + \Gamma(120°)(|H_2|^2 + |H_3|^2)]H_1. \tag{3}$$

Thereby β is a second order coupling coefficient and $\Gamma(\theta)$ is the cubic cross coupling coefficient, which depends on the angle between the interacting modes. Moreover, the stars denote complex conjugation. The corresponding equations for H_1 and H_2 follow by permutation of the indices. The term of cubic order is crucial for saturation. A linear stability analysis of the finite amplitude stationary solution $|H_1| = |H_2| = |H_3|$ noted in Ref. [8] yields a backwards bifurcation out of the trivial solution $H_i = 0$. This reflects a hysteretic transition from the undisturbed flat surface to a pattern of hexagons. However, we were unable to resolve any hysteresis because of small amplitude (harmonically oscillating) meniscus waves emitted from the rim of the container.

B. Theoretical model for the primary square pattern at $f > f_b$

Understanding the pattern selection process at the subharmonic side of the bicritical point is more complicated. Since the frequency spectrum of the subharmonic Faraday response consists of half integer multiples of f, any triple of linear unstable modes is prevented from resonating. Thus nonlinear pattern selection is dominated by a mechanism where the linear unstable modes resonate with their higher harmonics. Unlike triad resonances, which operate exclusively at an interaction angle of $\theta = 120°$, these resonances are less selective as they work at arbitrary angles θ. This fact is also reflected by the corresponding system of amplitude equations. Taking a set of N standing waves with wave numbers $\mathbf{k}_{S_i}$ at length $|\mathbf{k}_{S_i}| = k_c^s$ but arbitrary relative orientation, the respective mode amplitudes S_i are governed by the following evolution equations:

$$\partial_t S_i = \varepsilon S_i - \sum_{j=1}^{N} \Gamma(\theta_{ij}) |S_j|^2 S_i, \tag{4}$$

with θ_{ij} being the angle between $\mathbf{k}_{S_i}$, $\mathbf{k}_{S_j}$. Usually the participating modes are taken to be equidistant on the circle $|\mathbf{k}_{S_i}| = k_c^s$, thus $\theta_{i,i+1} = 2\pi/N$. In this case N indicates the type of symmetry of the pattern, namely $N = 1$ lines, $N = 2$ squares, $N = 3$ triangles or hexagons, ... As outlined in Refs. [22–25] the question of what is the most preferred symmetry is reduced to minimizing the "free energy"

$$F = -\varepsilon \sum_{i=1}^{N} |S_i| + \frac{1}{2} \sum_{i,j=1}^{N} \Gamma(\theta_{ij}) |S_i|^2 |S_j|^2 \tag{5}$$

with respect to N at given $\Gamma(\theta)$. For low viscosity fluid layers of infinite depth the coupling function $\Gamma(\theta)$ was first evaluated by Zhang and Viñals in 1997 [24], who found that a pattern of square symmetry is the most preferred one at drive frequencies beyond $f \approx 50$ Hz. At lower frequencies patterns with a degree of rotational symmetry up $N = 7$ (quasiperiodic) are likely to occur. These predictions were found to be in good agreement with experiments [26–28]. In Ref. [28] the considerations above are even extended to the case of finite fill heights and it was found that square patterns dominate also at lower drive frequencies in agreement with their own experiments and also with ours.

V. SECONDARY AND HIGHER ORDER TRANSITIONS AT $f < f_b$

A. Hexagon-square transition

In this section we investigate the crossover from the primary hexagonal structure (region V in Fig. 4) to the square pattern of region VI of the harmonic regime. Throughout the whole bifurcation cascade the time dependence is purely harmonic without perceptible subharmonic frequency contributions. The results described below were obtained by ramping the drive amplitude $\varepsilon = -0.01$ up to $\varepsilon = 0.165$ while keeping the frequency $f = 6.25$ Hz fixed (see Fig. 5). The transition is connected with a strong hysteresis giving an overlap between
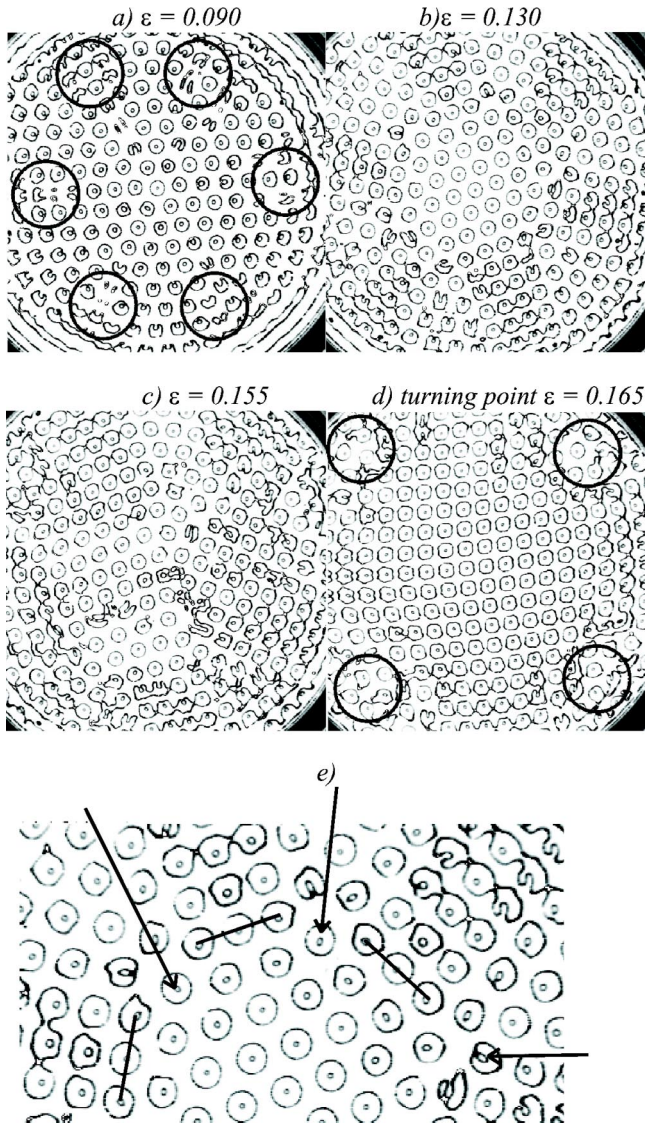
FIG. 5. Photographs of the fluid surface as obtained by ramping the drive amplitude ε at $f = 6.25$ Hz. The field of view is 26 $\times$ 26 cm and in the corners of the pictures the container boundary is visible. In (a) and (d) circles mark the nuclei at which the transition process is initiated. (e) is an enlarged sector of (b) with marked pentalines and hepta defects.

FIG. 6. (a) Surface area covered with squares $\mathcal{A}_4$ related to surface area of squares and hexagons $\mathcal{A}_6$ as function of the drive strength ε at the frequency $f = 6.25$ Hz. (b) The autocorrelation function $C(\phi = 90°)$ of the power spectra $P(\mathbf{k})$ on the circle ($|k| = k_c$). Upright (reversed) triangles refer to the upwards (downwards) amplitude ramp.

the two ideal structures. Since the lateral aspect ratio (container size over wavelength) is not large the hexagonal pattern adapts to an azimuthal symmetry. This affects the defect dynamic of the pattern and thereby also the transition process. Starting the ε ramp at the hexagonal structure, a rearrangement of the pattern sets in, initiated by six nuclei of local quadratic order as indicated by the circles in Fig. 5(a). The size of these patches increases with ε [Fig. 5(b)]. Conversely, starting at elevated ε with the perfect square pattern and ramping downwards generates four nuclei of local hexagonal order [Fig. 5(d)]. Along the domain boundaries between the patches penta-hepta defects occur. This kind of defect is very common in 2D hexagonal patterns. Experimental [8,29] and theoretical [30] investigations reveal that a penta-hepta defect can be formed by a phase defect among

two of the participating modes. Figure 5(e) presents an enlarged subrange of Fig. 5(b) depicting ''pentalines.'' This is a row of pentadefects (unit cells with five neighbors) ending in heptadefects (unit cells with seven neighbors). Strengthening the drive makes the domain walls invade the areas of hexagonal symmetry with new quadratic cells being generated along the penta lines.

To quantify the hysteresis of the hexagonal quadratic reconstruction we applied two different techniques, one in real space and the other in Fourier space. In the former case the number of unit cells with four neighbors $\mathcal{A}_4$ and those with six neighbors $\mathcal{A}_6$ was counted. The result of this procedure is shown in Fig. 6(a). It reveals a hysteresis loop extending from $\varepsilon = 0.05 \pm 0.01$ up to $\varepsilon = 0.15 \pm 0.01$. The obvious staircase behavior reflects the discretization of the k values due to the finite size of the container. For different runs the steps do not occur at the same ε values.

The second method for evaluating the square-vs-hexagon surface coverage follows an approach given in Ref. [27]. We Fourier transformed the full surface picture and evaluated the power spectrum $P(\mathbf{k}) = P(k, \phi)$ at $|\mathbf{k}| = k_c$ as a function of the azimuthal angle ϕ. We then computed the azimuthal auto correlation $C(\phi)$ as follows:

$$C(\phi) = \frac{\int_0^\pi P(k_c, \phi) P(k_c, \phi + \phi') d\phi'}{\int_0^\pi [P(k_c, \phi')]^2 d\phi'}. \quad (6)$$

That way a pattern with quadratic symmetry leads to a peak at $\phi = 90°$ and $180°$, while a hexagonal pattern produces maxima at $\phi = 60°$, $120°$ and $180°$.

Figure 7 illustrates how $C(\phi)$ develops with the drive amplitude, both at increasing and decreasing ε. In order to compare with the cell counting method [see Fig. 6(a)] the
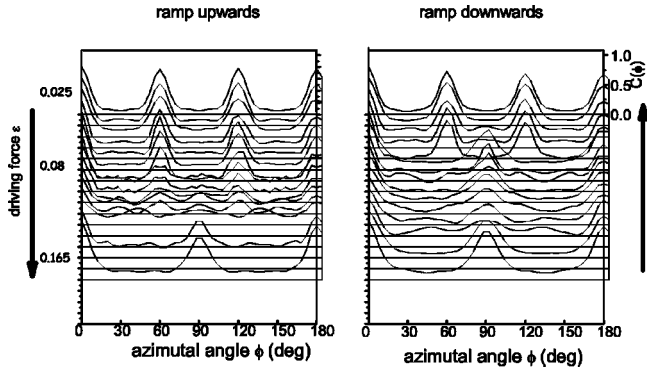
FIG. 7. Azimuthal autocorrelation $C(\phi)$ derived from the power spectra $P(\mathbf{k})$ at the wave number $|\mathbf{k}|=k_c$ as a function of the drive amplitude ε for ramping up and down.

value $C(\phi=90°)$ is plotted versus ε in Fig. 6(b). Regarding the width of the hysteresis loop, the two methods agree within a few percent with each other.

An important feature of the above phase transition is the constancy of the wave number $k^h(\varepsilon)=k_c^h$: Within the experimental resolution of $\Delta k/k=\pm 1\%$ no dependency of the wave number on ε could be detected throughout the whole investigated drive amplitude range. This is of particular significance as it allows to describe the global aspects of the phase transition in terms of a simple model as given in the next section.

B. Comparison with theory

It was outlined in Sec. IV that the hexagonal symmetry at small ε is a consequence of a three wave resonance, reflected by the second order term in Eq. (3). However, upon increasing the control parameter ε the term of cubic order becomes increasingly important, thus finally enforcing the transition towards squares. A minimal model that allows stationary solutions in form of squares and hexagons (and also lines) along with a linear stability analysis of these solutions can be found, e.g., in an analysis by Regnier [31]. This model is an extension of Eq. (3) as it relies on six independent modes $\mathbf{k}_i$ $(i=1,\ldots,6)$ rather than only three. Regnier finds that hexagons become unstable for a certain $\varepsilon>\epsilon_H$. By way of contrast, for a critical value of $\varepsilon<\epsilon_S$ squares become unstable.

It is tempting to attribute the bistable square-hexagon region in the theoretical bifurcation diagram between $\epsilon_S<\varepsilon <\epsilon_H$ to the hysteretic region depicted in Figs. 5(b) and 5(c). Note, however, that the observed transition runs through a reconstruction via penta-hepta defects, the complicated space dependence of which goes beyond the scope of the present model.

We mention that a discussion of a transition between hexagons and lines in terms of the above three mode model (3) has been given earlier in the context of Rayleigh-Bénard convection [7,8]. Thereby the phase transition results from non-Boussinesq effects induced by a strong applied temperature gradient. In the last decade, several authors report Bénard-Marangoni experiments, which show a transition from hexagons to squares [9–11]. A similar transition is found in Ref. [32] on the surface instability of magnetic liq-
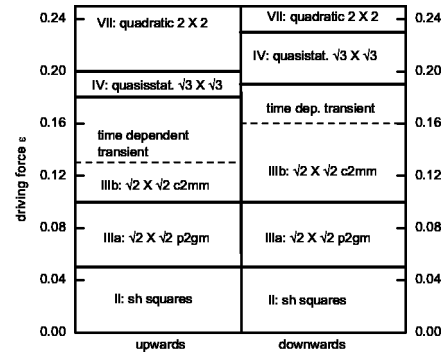
FIG. 8. Phase diagram of an amplitude scan at $f=7.25$ Hz. Time dependent transient means an uncorrelated pattern (Fig. 12), quasistationary indicates a pattern of an almost perfect $\sqrt{3}\times\sqrt{3}$ superlattice (compare Fig. 13) with a slow defect dynamic.

uids (Rosensweig instability). However, unlike our measurements, all of the aforementioned experiments with a hexagon to square transition exhibit a considerable nonlinear wave number variation $k(\varepsilon)$ up to 10%, which rules out a description in terms of space independent amplitude equations of the type given above. Our experiments allow for a description in terms of Landau equations and a model set of quantitative experimental data regarding the phase boundaries now exist. This provides the opportunity for an explicit comparison with a more detailed theoretical analysis.

VI. SECONDARY AND HIGHER TRANSITIONS AT $f>f_b$

In the same way as in the preceding paragraph we now turn to the bifurcation scenario at the opposite side of the bicritical point at $f>f_b$. An amplitude ramp taken at $f =7.25$ Hz serves as a representative example. Section VI D is an exception, where the focus is on the frequency regime 6.6 Hz$<f<$6.9 Hz.

An overview of the transition behavior at $f=7.25$ Hz is given by Figs. 8 and 9. Starting from subharmonic oscillating squares [region II, Fig. 9(a)] a transition to a quadratic $\sqrt{2} \times\sqrt{2}$ superlattice with a displacement of neighboring elevation maxima in the lateral x direction [region IIIa, Fig. 9(c)] takes place. The next pattern is again a $\sqrt{2}\times\sqrt{2}$ superlattice of the original square lattice but this time it exhibits a displacement in both x and y direction [region IIIb, Fig. 9(e)]. After a time dependent transient (see Fig. 12 for a snapshot) this pattern transforms into a "quasistationary" hexagonal $\sqrt{3}\times\sqrt{3}$ superlattice (region IV, Fig. 13). By "quasistationary" we indicate that the pattern is slightly disturbed by defects, which induce a slow time dependence on the scale of minutes. Further raising the drive amplitude ε at $f =7.25$ Hz makes the quadratic symmetry reappear in the form of a 2×2 superlattice (region VII, Fig. 14). Performing the same amplitude ramp at a lower frequency of 6.6 Hz $<f<$6.9 Hz the $\sqrt{3}\times\sqrt{3}$ superlattice directly reduces to its underlying pure hexagonal tiling. This last transition will be discussed in Sec. VI D.
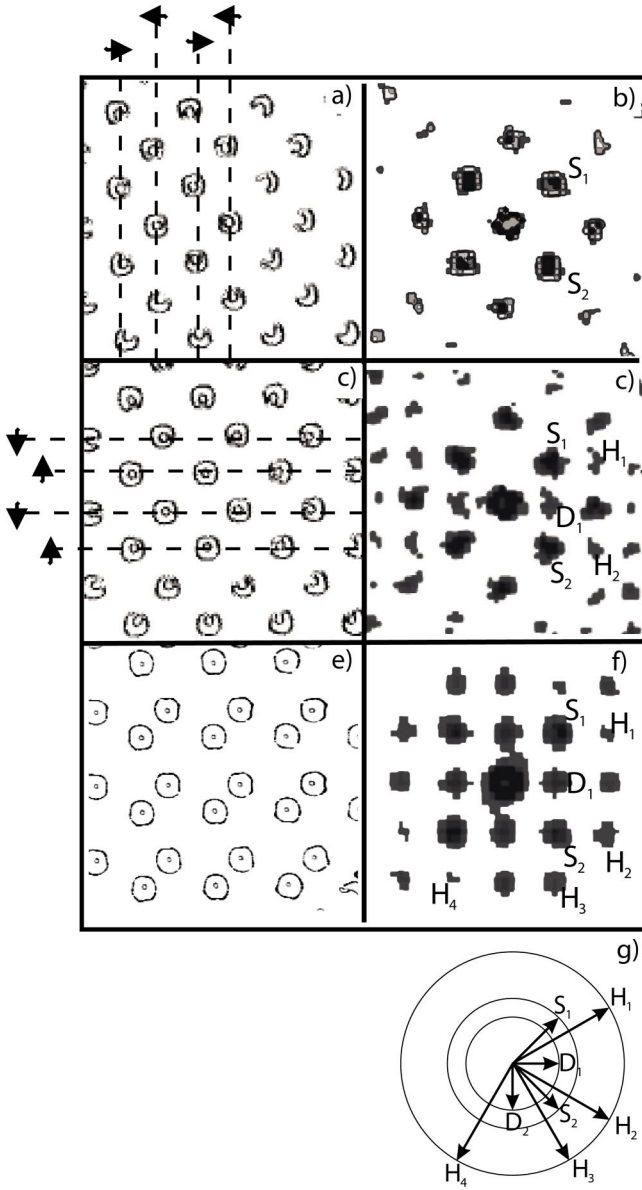
FIG. 9. A 10×10 cm sector of the photographs of the fluid surface and a quadratic sector (ranging from -1280 m^{-1} to 1280 m^{-1}) of the contour plot representation of the corresponding Fourier spectra of the complete surface area at $f = 7.25$ Hz. (a),(b): $\varepsilon = 0.03$, region II, pattern of squares; (c),(d): $\varepsilon = 0.07$, region IIIa, $\sqrt{2} \times \sqrt{2}$ superlattice p2mg with a displacive character in x direction; (e),(f): $\varepsilon = 0.14$ $\sqrt{2} \times \sqrt{2}$, region IIIb, superlattice c2mm with a displacive character in x and y direction. The dotted lines and arrows on the left pictures indicate the directions in which the rows and columns of elevation maxima are displaced on the image below. (g) Minimal set of Fourier modes that are necessary to generate the observed surface states.

A. The quadratic $\sqrt{2} \times \sqrt{2}$ superlattice

The bifurcation sequence starts at the primary ideal pattern of subharmonically oscillating squares [region II and Figs. 9(a) and 9(b)] composed of the two fundamental wave vectors $\mathbf{k}_{S_1}$ and $\mathbf{k}_{S_2}$. Increasing the drive strength ε beyond 0.05 displaces every other column of elevation maxima in
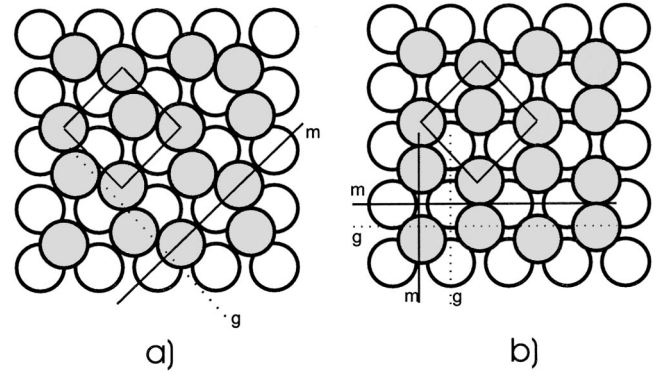
FIG. 10. Particle model of the (a) $\sqrt{2} \times \sqrt{2}$ p2mg and (b) $\sqrt{2} \times \sqrt{2}$ c2mm superlattice. Also marked are the mirror (m) and glide (g) planes.

the direction $\pm(\mathbf{k}_{S_1} + \mathbf{k}_{S_2})$. This is shown by the arrows in Fig. 9(a). The resulting pattern (phase region IIIa) is depicted in Fig. 9(c). The displacement is accompanied by the simultaneous appearance of the modes $\mathbf{k}_{H_1}$, $\mathbf{k}_{H_2}$, and $\mathbf{k}_{D_1}$ in the power spectrum [see Fig. 9(d)]. Due to the approximate equality $|\mathbf{k}_{H_1}| = |\mathbf{k}_{H_2}| \simeq k_c^h$ these modes are only slightly damped. In contrast, $|\mathbf{k}_{D_1}|$ is significantly smaller than k_c^s and k_c^h. Therefore the mode D_1 is strongly damped. Its mission is to act as a mediator mode, enabling the resonance between S and H modes according to the geometrical rules $\mathbf{k}_{H_1} = (\mathbf{k}_{S_1} + \mathbf{k}_{D_1})$ and $\mathbf{k}_{H_2} = (\mathbf{k}_{S_2} + \mathbf{k}_{D_1})$. This implies that $\mathbf{k}_{D_1}$ must be associated with a subharmonic time dependence. Moreover, it follows from $k_c^h/k_c^s \simeq 1.58$ that $|\mathbf{k}_{D_1}| = 0.71 \simeq 1/\sqrt{2}$, which leads to the commensurate relationship $\mathbf{k}_{D_1} \simeq \frac{1}{2}(\mathbf{k}_{S_1} + \mathbf{k}_{S_2})$ for the new fundamental wave vector. The corresponding elementary cell [see Fig. 10(a)] is rotated by 45° relative to the original quadratic grid, and the basic wavelength is enlarged by a factor of $\sqrt{2}$. We therefore denote this pattern as a $\sqrt{2} \times \sqrt{2}$ superlattice [more precisely, $(\sqrt{2} \times \sqrt{2})R45$ or $\sqrt{2} \times \sqrt{2}$ $p2mg$ in the nomenclature of space group theory (see Ref. [38])]. It turns out that the displacive character of the superlattice is inherent in the phase information carried by the participating modes. Barring higher spatial harmonics the space dependence of the surface deformation shown in Fig. 9 can be expressed as

$$\zeta(\mathbf{r}) = \sum_{i=1}^{2} S_i \cos(\mathbf{k}_{S_i} \cdot \mathbf{r} + \phi_{S_i}) + D_1 \cos(\mathbf{k}_{D_1} \cdot \mathbf{r} + \phi_{D_1})$$
$$+ \sum_{i=1}^{2} H_i \cos(\mathbf{k}_{H_i} \cdot \mathbf{r} + \phi_{H_i}). \quad (7)$$

Equation (7) is a special case of the spatial part of Eq. (2) with D_1 as an additional variable for a specific Fourier amplitude for a better structuring. By means of the ray tracing technique outlined in Sec. I B we can now simulate the video image associated with $\zeta(\mathbf{r})$ and adapt it to the empiric result. Taking $\phi_{S_1} = \phi_{S_2} = 0$ (by a proper choice of the origin) our investigation reveals that the displacement visible in Fig.
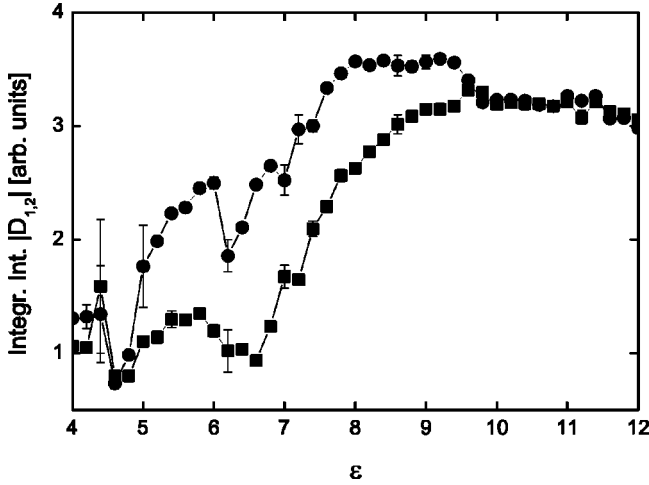
FIG. 11. Integrated intensity of the D_1 peak (circles) and the D_2 peak (squares) in the power spectrum as a function of the drive amplitude ε. The error bars mark the standard derivation resulting from five succeeding runs.

9(b) can only be reproduced if the spatial phases ϕ_{D_1}, ϕ_{H_1}, and ϕ_{H_2} adopt values close to $=\pi/2$. The associated surface pattern exhibits a 180° rotational symmetry.

By increasing the drive further the $\sqrt{2}\times\sqrt{2}\ p2mg$ superlattice undergoes a transition which restores the fourfold symmetry. Similar to the above described shift of the *columns* of elevation maxima, it is now additionally the *rows*, which experience a displacement in the direction $\pm(\mathbf{k}_{S_1}-\mathbf{k}_{S_2})$ [indicated by the arrows in Fig. 9(c)]. In Fig. 11 we measured the amount of symmetry restoration by comparing the spectral power associated with D_1 and D_2. Beyond $\varepsilon \simeq 9\%$ the transition is complete. The resulting so called $\sqrt{2}\times\sqrt{2}\ c2mm$ superlattice [see Fig. 10(b)] is depicted in Fig. 9(e) and associated with the phase space region IIIb. In Fourier space this transition is carried by the additional modes $\mathbf{k}_{H_3}$, $\mathbf{k}_{H_4}$ and $\mathbf{k}_{D_2}$ as shown in Fig. 9(f). Extending the surface representation equation (7) by these additional components and using it to reperform the ray tracing image analysis yields the phase information ϕ_{D_i} ($i=1,2$) $=\phi_{H_i}$ ($i=1,\ldots,4$) $=\pi/2$.

We mention that the $\sqrt{2}\times\sqrt{2}\ c2mm$ superlattice state was not observed in an earlier measurement on a liquid of higher viscosity [6]. Thereby this structure is preempted by a transition to a hexagonal symmetry.

B. Theoretical model for the displacive phase

The experimental investigations outlined in the previous section reveal that the prominent displacive character of the $\sqrt{2}\times\sqrt{2}$ superlattices is associated with the phase information carried by the spatial Fourier modes. In what follows, a minimal model is constructed, which is able to explain the experimentally measured phases. It is important to point out that the *structure* of these equations just relies on symmetry and resonance arguments (triad wave vector resonances). The *numerical values* of the appearing coefficients are not

known; their evaluation would require a rather complicated nonlinear analysis. A formal proof is still missing if a description in terms of amplitude equations is justified at all, taking the elevated driving strength ϵ in our experiments into account. However, the patterns consisting of well-defined Fourier components and the surprisingly good agreement between the predicted and measured prominent spatial phases render the following analysis very instructive. For the sake of simplicity, we limit our discussion to the $\sqrt{2}\times\sqrt{2}\,p2mg$ superlattice. The generalization to the more symmetric $\sqrt{2}\times\sqrt{2}\,c2mm$ pattern is straightforward.

Assuming that the amplitudes of the primary square pattern have settled at some finite value $S_1=S_2\neq 0$ the leading order behavior of the remaining modes is governed by the following set of equations:

$$\partial_t D_1 = \varepsilon_D D_1 + \mu_D(S_1^\star H_1 + S_2^\star H_2) + \chi_S S_1 S_2 D_1^\star,$$

$$\partial_t H_1 = \varepsilon_H H_1 + \mu_H S_1 D_1, \qquad (8)$$

$$\partial_t H_2 = \varepsilon_H H_2 + \mu_H S_2 D_1.$$

Thereby $\varepsilon_H < 0$ and $\varepsilon_D \ll 0$ are the coefficients of linear damping of the H and D modes, respectively, while $\mu_{D,H}$ and χ_S are nonlinear coupling coefficients associated with the triad wave vector resonance.

Although the model equations (8) are linear in D and H and thus saturation is not implied, the appearing nonlinearities are phase selective. By writing the complex amplitudes in the form $A_i=|A_i|\exp(\phi_{A_i})$ with again $\phi_{S1}=\phi_{S2}$ taken to be zero (choice of space origin) the imaginary part of Eq. (8) yields the phase dynamics

$$\partial_t \phi_{D_1} = \mu_D |S||H|/|D|[\sin(\phi_{H_1}-\phi_{D_1}) + \sin(\phi_{H_2}-\phi_{D_1})]$$
$$+ \chi_S |S|^2 \sin(-2\phi_{D_1}),$$

$$\partial_t \phi_{H_1} = \mu_H |D||S|/|H|\sin(\phi_{D_1}-\phi_{H_1}), \qquad (9)$$

$$\partial_t \phi_{H_2} = \mu_H |D||S|/|H|\sin(\phi_{D_1}-\phi_{H_2}).$$

The fix points of these equations are

$$\phi_{H_i} = \phi_{D_i} = m\frac{\pi}{2} \qquad (10)$$

with m being an integer. By inspection one finds that the solution with even m leads to a square pattern with *amplitude modulation* while odd m gives rise to the observed displacement (*phase modulation*). Which one is stable, depends on the numeric values of the coefficients. From the experimental data we conclude that $\phi_{H_i}=\phi_{D_i}=\pi/2$ is the solution applicable to the present experiment.

C. The hexagonal $\sqrt{3}\times\sqrt{3}$ superlattice

Upon further increase of the driving force at $f=7.25$ Hz the quadratic $\sqrt{2}\times\sqrt{2}c2mm$ superlattice transforms into a "quasistationary" hexagonal superlattice (region IV, com-
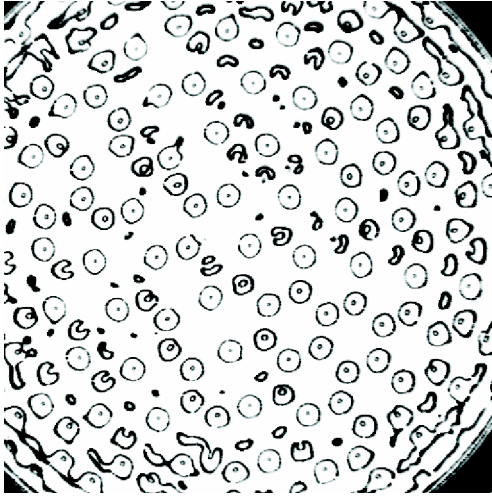
FIG. 12. Snapshot of the fluid surface as obtained at $f = 7.25$ Hz and $\varepsilon = 0.17$. The field of view is 26×26 cm. The pattern is strongly time dependent and spatially uncorrelated.

pare Fig. 13) after passing a region of transient time dependent (Fig. 12) with squares, hexagons and disordered patterns appearing at the same value of ε. The term "quasistationary" is to indicate that the pattern is affected by defects on a slow time scale of minutes. The power spectrum shown in Fig. 13(b) reveals that the structure is composed of a set of three harmonic modes H_j and three subharmonic modes S_j. The angles between the wave vectors of the three H modes is 120° and so is the angle of the S modes. The H pattern is rotated by 30° and locked in phase with respect to the S pattern, the ratio k_h / k_s is $1.73 \simeq \sqrt{3}$. Therefore the pattern is denoted as a $\sqrt{3} \times \sqrt{3}$ superlattice. We mention an earlier investigation on a more viscous fluid of $\nu = 10$ cS (cf. [6]): Thereby the transition from the quadratic $\sqrt{2} \times \sqrt{2}$ $p2mg$ to the hexagonal $\sqrt{3} \times \sqrt{3}$ superlattice took place in a more correlated manner via stacking faults while the $\sqrt{2} \times \sqrt{2}$ $c2mm$ state could not be observed.
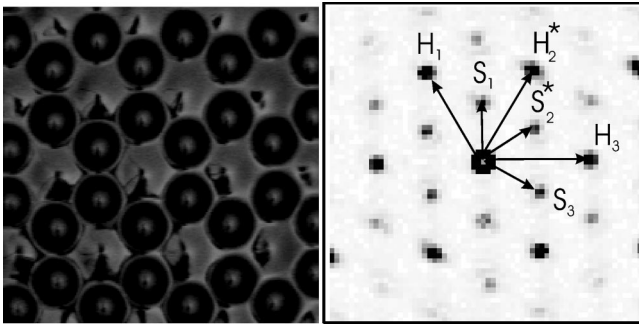
FIG. 13. An 8×8 cm sector of the photographs of the fluid surface and a quadratic sector (ranging from -760 m^{-1} to 760 m^{-1}) of the corresponding gray density plot representation of the Fourier spectra of the complete surface area at $f = 6.65$ Hz and $\varepsilon = 0.05$. This photograph has been obtained by using a diffusive light source mounted off axis instead of the standard visualization technique. In that way the character of the hexagonal $\sqrt{3} \times \sqrt{3}$ superlattice (region IV) appears to be more pronounced [compare Fig. 4(e) in Wagner (2000)].
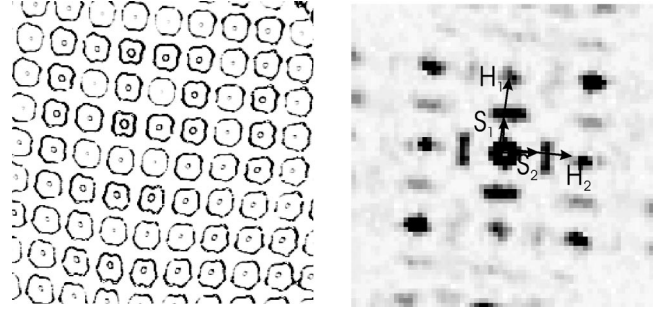
FIG. 14. An 8×8 cm sector of the quadratic 2×2 superlattice and a quadratic sector (ranging from -1080 m^{-1} to 1080 m^{-1}) of the corresponding gray density plot representation of the Fourier spectra of the complete surface area at $f = 7.25$ Hz and $\varepsilon = 0.24$ (region VII).

At higher ε values the further development of the $\sqrt{3} \times \sqrt{3}$ superlattice depends on the drive frequency: At 6.6 Hz$< f <$6.9 Hz, where the superlattice is perfectly stationary and almost free of defects, the amplitude of the subharmonic components of the structure continuously become smaller until the hexagonal base pattern with a pure synchronous time dependence remains [region V, compare Fig. 5(a)]. This transition is slightly hysteretic ($\Delta \varepsilon \simeq 0.01 - 0.02$) and can be localized accurately by means of the triggering technique described in Sec. I. We come back to this crossover in Sec. VI D, in order to present a theoretical model.

At drive frequencies larger than $f \approx 6.9$ Hz (for concreteness let us return to our run at $f = 7.25$ Hz) the hexagonal $\sqrt{3} \times \sqrt{3}$ superstructure transforms into a 2×2 superlattice (region IV $\rightarrow$ VII) thereby restoring the quadratic symmetry. The crossover takes place via a spatially weakly correlated transient, being subjected to a strong temporal dynamic. The corresponding pattern looks similar to the surface state shown in Fig. 12. In its final state the subharmonic and the harmonic wave vectors $\mathbf{k}_{S,H}$ are aligned with each other [Fig. 14(b)]. With $k^h \approx k_c^h$ but $k^s \approx 0.8 k_c^s$ the resulting length ratio k_H / k_S is about 2.

D. Theoretical model for the $\sqrt{3} \times \sqrt{3}$ superlattice-to-hexagon transition

A model of amplitude equations for the $\sqrt{3} \times \sqrt{3}$ superlattice (region IV) can be easily constructed similar to Eq. (8). Again the spatial phases are of most interest, because they determine the detailed appearance of the pattern. For the underlying harmonic hexagonal structure with amplitudes $H_i = |H_i| \exp(i\Phi_{H_i})$ one finds by analyzing terms of quadratic order either $\Phi_H = \Sigma_j^3 \phi_{H_j} = 0$ or π, corresponding respectively to "up" or "down" hexagons. For Faraday waves this distinction is not significant because the surface oscillation periodically switches between these two possible states. Splitting the subharmonic mode amplitudes also into modulus and phase and assuming without loss of generality that $\phi_{H_1} = \phi_{H_2} = 0$, one finds in quadratic order $\phi_{S_1} = \phi_{S_2} = \phi_{S_3}$. In order to determine that value it is necessary to proceed with the amplitude expansion up to the quintic order, yielding

$$\Phi_S = n\pi/2, \tag{11}$$

where n is an integer and with the parametrization $\Phi_S = \Sigma_j^3 \phi_{S_j} = 3\phi_{S_i}$. Following the usual nomenclature the pattern with odd n is a triangular superlattice, as its rotational symmetry is threefold. For even n the superlattice exhibits a sixfold symmetry (cf. [33]). Since a sixfold symmetry center can be easily identified in Fig. 13, we conclude that n is even in our experiment. We point out that an example of a $\sqrt{3} \times \sqrt{3}$ with third order rotational symmetry (n is odd) has recently been observed by Pi *et al.* [34] (see also Ref. [35]).

VII. CONCLUSIONS

We have presented a comprehensive investigation on Faraday wave pattern formation in the vicinity of a bicritical situation. In contrast to many other experiments we used a single frequency drive and the bicritical situation was obtained by working at low frequencies with a thin layer of liquid. The use of a single driving frequency limits the external parameters and the theoretical analysis remains simpler. Nevertheless, the interaction of the modes with harmonic and subharmonic time dependence lead to a variety of new superlattice states. This kind of structure acts as a mediator during the transition process between two incompatible space groups (squares and hexagons). We developed several sets of amplitude equations to model the observed phase transitions. Special attention is devoted to the phase information carried by the participating modes, which is responsible for the remarkable displacive feature of one of the superlattices. The primary subharmonic square pattern evolves with onset of the harmonic branch into a $\sqrt{2} \times \sqrt{2}$ superlattice with a displacive character in first one and with increasing drive strength in two perpendicular directions. And the transition to the hexagonal harmonical oscillating phase develops via a $\sqrt{3} \times \sqrt{3}$ superlattice.

Superlattices are rather common in 2D solid state physics, and a comparison is therefore instructive. The transition from a simple hexagonal lattice to a $\sqrt{3} \times \sqrt{3}$ superstructure has been observed for instance in monolayers of C_2ClF_5 adsorbed on graphite [36]. The transition from the subharmonic quadratic base pattern to a $\sqrt{2} \times \sqrt{2}$ superlattice with a displacive character in one direction ($p2mg$, region IIIa) is analogous to the reconstruction of the clean (100) surface of W ($=$ tungsten) crystals [37]. Here the surface atoms are displaced in exactly the same way as the elevation maxima of the surface profile in the present study. Most interestingly, the surface of W crystals obeys a transition to a $\sqrt{2} \times \sqrt{2}$ superlattices with a displacive character in two directions ($c2mm$, identical to our pattern in region IIIb) in the presence of hydrogen atoms.

We were also able to provide for the first time a pattern forming system, which undergoes a hexagon-to-square transition without a simultaneous change of the fundamental wavelength. This is in contrast to earlier observations on the Bénard-Marangoni system, which showed considerable wave number variations during the transition process. The accompanying description in terms of well-defined spatial Fourier modes makes the phase transition very fundamental and identifies the underlying pattern selection mechanism to switch from a triad to a four-wave vector resonance.

---

[1] M. Faraday, Philos. Trans. R. Soc. London **52**, 319 (1831). For a review, see J.W. Miles and D. Henderson, Annu. Rev. Fluid Mech. **22**, 143 (1990); H.W. Müller, R. Friedrich, and D. Papathanassiou, in *Evolution of Stuctures in Dissipative Continuous Systems*, edited by F. Busse and S.C. Müller (Springer, Berlin, 1998), Vol. 55.

[2] T.B. Benjamin and F. Ursell, Proc. R. Soc. London, Ser. A **225**, 505 (1954).

[3] W.S. Edwards and S. Fauve, J. Fluid Mech. **278**, 123 (1994).

[4] K. Kumar, Proc. R. Soc. London, Ser. A **452**, 1113 (1996).

[5] H.W. Müller, H. Witmer, C. Wagner, J. Albers, and K. Knorr, Phys. Rev. Lett. **78**, 2357 (1997).

[6] C. Wagner, H.W. Müller, and K. Knorr, Phys. Rev. E **62**, R33 (2000).

[7] R.W. Walden and G. Ahlers, J. Fluid Mech. **109**, 89 (1981).

[8] S. Ciliberto, E. Pampaloni, and C. Pérez-García, Phys. Rev. Lett. **61**, 1198 (1988).

[9] K. Nitschke and A. Thess, Phys. Rev. E **52**, R5772 (1995).

[10] M. Bestehorn, Phys. Rev. Lett. **76**, 46 (1996).

[11] K. Eckert, M. Bestehorn, and A. Thess, J. Fluid Mech. **356**, 155 (1998).

[12] M.F. Schatz and M.F. Neitzel, Annu. Rev. Fluid Mech. **33**, 93 (2001).

[13] E. Pampaloni, S. Residori, S. Soria, and F.T. Arecchi, Phys. Rev. Lett. **78**, 1042 (1997).

[14] A. Kudrolli, B. Pier, and J.P. Gollub, Physica D **123**, 99 (1998).

[15] H. Arbell and J. Fineberg, Phys. Rev. Lett. **81**, 4384 (1998); H. Arbell and J. Fineberg, Phys. Rev. E **65**, 036224 (2002).

[16] C. Wagner, H.W. Müller, and K. Knorr, Phys. Rev. Lett. **83**, 308 (1999).

[17] W. Zhang and J. Viñals, J. Fluid Mech. **225**, 222 (1997); B. Dionne, M. Silber, and A.C. Skeldon, Nonlinearity **10**, 321 (1997); M. Silber and A.C. Skeldon, Phys. Rev. E **59**, 5446 (1999); J. Porter and M. Silber, Phys. Rev. Lett. **89**, 084501 (2002); M. Silber, A.C. Skeldon, and C.M. Topaz, Physica D **172**, 1 (2002).

[18] Lord Rayleigh, Philos. Mag. **5**, 229 (1883).

[19] E. Cerda and E. Tirapegui, Phys. Rev. Lett. **78**, 859 (1997).

[20] K. Kumar and L. Tuckerman, J. Fluid Mech. **279**, 49 (1994).

[21] A. Wernet, C. Wagner, D. Papathanassiou, H.W. Müller, and K. Knorr, Phys. Rev. E **63**, 036305/1 (2001).

[22] S.T. Milner, J. Fluid Mech. **225**, 81 (1991).

[23] H.W. Müller, Phys. Rev. E **49**, 1273 (1994).

[24] W. Zhang and J. Viñals, Phys. Rev. E **53**, R4283 (1997).

[25] P. Chen and J. Viñals, Phys. Rev. Lett. **79**, 2670 (1997); P. Chen and J. Viñals, Phys. Rev. E **60**, 559 (1999).

[26] A. Kudrolli and J.P. Gollub, Physica D **97**, 133 (1996).

[27] D. Binks and W. van de Water, Phys. Rev. Lett. **78**, 4043 (1997).

[28] D. Binks, M.T. Westra, and W. van de Water, Phys. Rev. Lett. **79**, 5010 (1997).

[29] T. Tam, D. Ohata, and M. Wu, Phys. Rev. E **61**, R9 (2000).

[30] S. Ciliberto, P. Coullet, J. Lega, E. Pampaloni, and C. Pérez-García, Phys. Rev. Lett. **65**, 2370 (1990); L.M. Pismen and A.A. Nepomnyashchy, Europhys. Lett. **24**, 461 (1993); L.S. Tsimring, Physica D **89**, 368 (2000); H. Herrero, C. Pérez-García, and M. Bestehorn, Chaos **4**, 15 (1994); C. Kubstrup, H. Herrero, and C. Pérez-García, Phys. Rev. E **54**, 1560 (1996).

[31] V. Regnier, P.C. Dauby, P. Parmentier, and G. Lebon, Phys. Rev. E **55**, 6860 (1997).

[32] B. Abou, J.E. Wesfreid, and S. Roux, J. Fluid Mech. **416**, 217 (2000).

[33] H.W. Müller, Phys. Rev. Lett. **71**, 3287 (1993).

[34] H.J. Pi, S. Park, J. Lee, and K.J. Lee, Phys. Rev. Lett. **84**, 5316 (2000).

[35] C. Wagner and H.W. Müller, Phys. Rev. Lett. **87**, 189401/1 (2001).

[36] S. Fassbender, C. Steimer, D. Arndt, and K. Knorr, Phys. Rev. Lett. **75**, 2526 (1995).

[37] G. Schmidt, H. Zagel, H. Landskorn, K. Heinz, K. Müller, and J.B. Pendry, Surf. Sci. **271**, 416 (1992).

[38] *International Tables for Crystallography*, edited by Theo Hahn (Reidel, Dordrecht, 1983), Vol. A.